

A 4 - 8 GHz Kinetic Inductance Travelling-Wave Parametric Amplifier Using Four-Wave Mixing with Near Quantum-Limit Noise Performance

Farzad Faramarzi,¹ Ryan Stephenson,^{2,1} Sasha Sypkens,^{1,3} Byeong H. Eom,¹ Henry LeDuc,¹ and Peter Day¹

¹*Jet Propulsion Laboratory, California Institute of Technology, Pasadena, CA 91101,*

USA

²*Division of Physics, Mathematics and Astronomy, California Institute of Technology, Pasadena, CA 91125,*

USA

³*School of Earth and Space Exploration, Arizona State University, Tempe, Arizona 85281,*

USA

(*Electronic mail: peter.k.day@jpl.nasa.gov)

(*Electronic mail: farzad.faramarzi@jpl.nasa.gov.)

(Dated: 14 March 2024)

Kinetic inductance traveling-wave parametric amplifiers (KI-TWPA) have a wide instantaneous bandwidth with near quantum-limited sensitivity and a relatively high dynamic range. Because of this, they are suitable readout devices for cryogenic detectors and superconducting qubits and have a variety of applications in quantum sensing. This work discusses the design, fabrication, and performance of a KI-TWPA based on four-wave mixing in a NbTiN microstrip transmission line. This device amplifies a signal band from 4 to 8 GHz without contamination from image tones, which are produced in a separate higher frequency band. The 4 - 8 GHz band is commonly used to read out cryogenic detectors, such as microwave kinetic inductance detectors (MKIDs) and Josephson junction-based qubits. We report a measured maximum gain of over 20 dB using four-wave mixing with a 1-dB gain compression point of -58 dBm at 15 dB of gain over that band. The bandwidth and peak gain are tunable by adjusting the pump-tone frequency and power. Using a Y-factor method, we measure an amplifier-added noise of $0.5 \leq N_{added} \leq 1.5$ photons from 4.5 - 8 GHz.

I. INTRODUCTION

Using a quantum noise-limited parametric amplifier as a first-stage amplifier for readout can improve the sensitivity of multiple cryogenic detector technologies, such as the Microwave Kinetic Inductance Detector (MKID)¹, and microwave SQUID multiplexer (μ MUX) readout of Mettalic Magnetic Calorimeters² and Transition-Edge Sensors³. Traveling wave parametric amplifiers are also an appealing choice for fast and high-fidelity readout⁴⁻⁶ of cryogenic qubits. A commonly used frequency band to read out superconducting qubits and detectors is 4 - 8 GHz due to its availability, accessibility, and maturity of readout electronic systems and components at a relatively low cost. Applications of superconducting parametric amplifiers also extend to fundamental physics research for laboratory-based experiments such as dark matter searches, where a quantum-noise-limited gain is of interest⁷.

The resonant Josephson junction amplifiers (JPAs) are the most commonly used superconducting parametric amplifiers⁸. Even though these devices have shown quantum-limited noise performance, they have low fractional bandwidths and very low dynamic range⁹. Recently, by implementing a traveling-wave periodic structure^{8,10}, the bandwidths of Josephson traveling-wave parametric amplifiers (JTWPAs) have been increased to a few gigahertz¹¹. However, the low dynamic range of these devices still remains an issue, especially for the readout of resonator arrays¹⁰. In addition, the complexity of circuitry of the nonlinear lumped element transmission line and junction fabrication also puts them at a disadvantage compared to their counterparts, the kinetic inductance-based parametric amplifiers¹²⁻¹⁹.

Kinetic inductance-based superconducting parametric am-

plifiers utilize the nonlinear kinetic inductance of superconducting thin films such as NbTiN. Four-wave mixing (4WM) processes can occur in kinetic inductance transmission line structures patterned in coplanar waveguide¹⁴ or microstrip line¹² geometries when a strong pump tone is present. A phase-matching condition is necessary to obtain maximum gain over a desired bandwidth. Implementing geometric dispersion allows for control of phase matching. This technique, called dispersion engineering, can also be utilized to mismatch unwanted higher-order nonlinear processes such as pump third harmonic¹⁴.

Three-wave mixing (3WM) is possible with KI-TWPAs when a constant current is applied to the transmission line. 3WM KI-TWPAs have demonstrated a near quantum-limited noise, wide bandwidth, and high dynamic range^{13,20}. However, since the pump tone corresponds to twice the frequency at the center of the gain curve, it is then folded about its center in the sense that a signal on one side of $f_{pump}/2$ produces an idler tone at the reflected frequency of $f_{pump} - f_{signal}$. That situation is far from ideal for reading out densely frequency-spaced arrays of resonators where the resulting frequency collisions would seriously impact the yield and other cases where there is power at frequencies corresponding to the idler part of the band. The total bandwidth of the published 3WM devices is also somewhat less than 4-8 GHz^{13,20}.

This paper presents a degenerate four-wave mixing KI-TWPA, where the pump tone is between the signal and idler frequencies, $2f_{pump} = f_{signal} + f_{idler}$. The amplifier tends to produce a gain in disjointed frequency ranges that we will refer to as the signal and idler (or image) bands, which makes it possible to separate the idler using ancillary circuitry and use the full signal band without contamination from the image (or idler) frequencies. The devices described here are made of

NbTiN and patterned in an inverted microstrip geometry¹². The transmission line is dispersion engineered by adding sinusoidally modulated capacitive stubs with a median length of $9.2 \mu\text{m}$ and modulation of $2.08 \mu\text{m}$ to create a bandgap centered at 12.5 GHz.

II. DEVICE DESIGN AND FABRICATION

The design of the device is similar to what was reported in Shu et al.¹² with the exception of Nb as the ground plane. To effectively increase the nonlinearity in the kinetic inductance of the transmission line as a function of the pump current (I_p), the transmission line width was designed to be 320 nm as shown in Fig. 1.a. The kinetic inductance per unit length as a function of pump current is given by the following relation¹⁴:

$$\mathcal{L}_k(I_p) = \mathcal{L}_k(I_p = 0) \left(1 + \frac{I_p^2}{I_*^2} + \dots \right), \quad (1)$$

where I_* is the “characteristic” current that sets the scale of the nonlinearity.

The increase in the impedance of the transmission line, $Z \approx \sqrt{\mathcal{L}_k/\mathcal{C}}$, due to its narrow width and large kinetic inductance was compensated for by adding capacitive stubs to increase the capacitance per unit length, \mathcal{C} , of the transmission line. The length of the stubs was set to create the dispersion needed for the four-wave mixing process and further modulated along the length of the transmission line to create a photonic bandgap¹⁴ around the pump frequency, as shown in Fig 1.b.

We can approach the following phase-matching criterion for a wide range of frequencies by putting the pump at the upward step before the bandgap:

$$\Delta\beta = \kappa_s + \kappa_i - 2\kappa_p = -\kappa_p \frac{I_p^2}{4I_*^2}, \quad (2)$$

where κ_s, κ_i , and κ_p are the wave vectors corresponding to the signal, idler, and pump tones, respectively, and the term on the right represents the nonlinear dispersive effect¹⁴. Fig. 1.c shows a plot of $\Delta\beta$ as a function of frequency.

The devices were fabricated by depositing a 35-nm thick NbTiN layer on a 6-inch high resistivity ($\rho \geq 10,000 \Omega\cdot\text{cm}$) silicon wafer via reactive sputtering from a NbTi target in a nitrogen atmosphere at ambient temperatures. The NbTiN film was then patterned using a stepper photo-lithography method, and then etched in a reactive ion etcher. Utilizing a Plasma-Enhanced Chemical Vapor Deposition (PECVD) process, a 60-nm thick amorphous silicon layer was deposited on top of the NbTiN wire. Finally, a 350-nm thick Nb ground-plane layer was sputtered on top of the amorphous silicon layer and then patterned and etched.

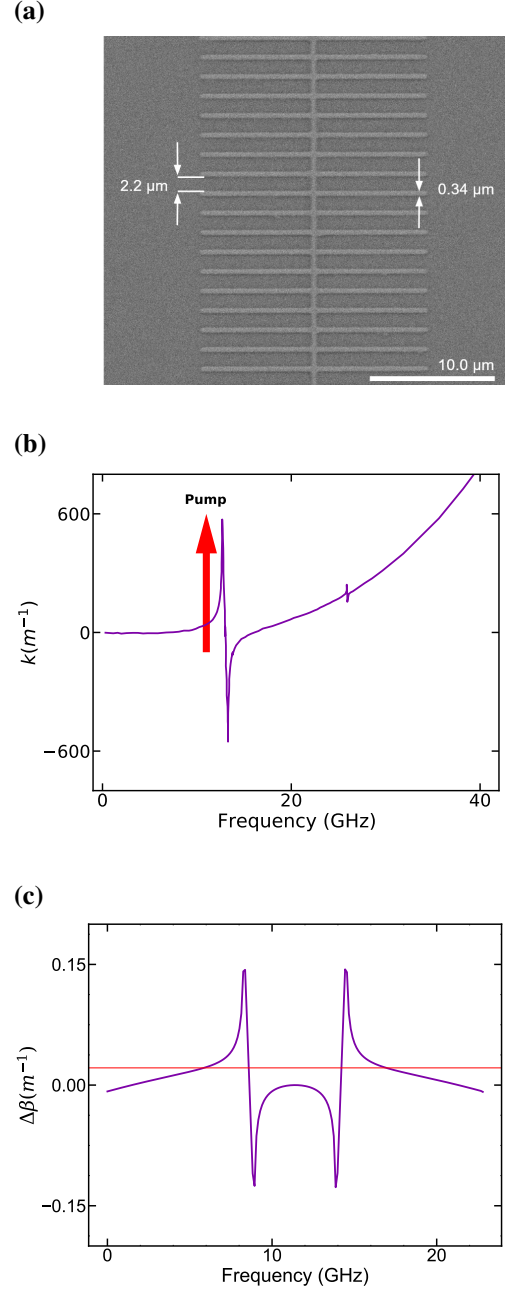


FIG. 1: a) A SEM micrograph of the transmission line with capacitive stubs. The width of the stubs is 340 nm, the spacing between them is 2.2 microns, and the average length of the stubs is 10.8 microns. b) Plot of the calculated propagation constant with a linear part subtracted as a function of frequency with a discontinuity at around 12.5 GHz, which results from the modulation of the length of the capacitive stubs with a periodicity of 122.7 microns. The inset shows the structure of the simulated dispersion around the bandgap and the position of the pump tone relative to the bandgap. c) Plot of calculated phase matching criterion, $\Delta\beta$, as a function of frequency. Shown in red is the self-phase modulation of the pump, $\kappa_p \frac{I_p^2}{4I_*^2}$, and in purple is the difference between the pump wave number, $2\kappa_p$, relative to the signal and idler wave numbers, κ_s and κ_i . The optimal parametric gain (maximum gain) is achieved near the outer intersecting points.

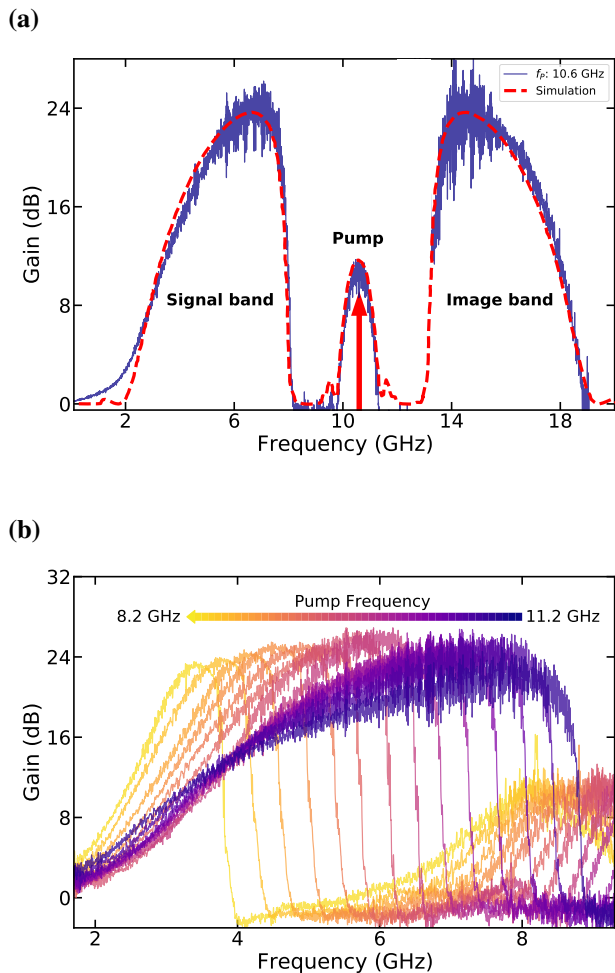


FIG. 2: a) Shows the measured gain of the device at 1 K with pump frequency at 10.6 GHz. The frequencies over which the device produces gain are split into three bands. The gap at around 12 GHz is due to the “engineered” band gap produced by the periodic modulation of the transmission line structure^{12,20}. The gap around 8 GHz corresponds to frequencies where the idler tone ends up in the band gap, so the 4WM process is inoperative. The dashed line shows the simulated gain curve with the same pump condition as the measured gain of the device. b) plot of measured gain of the device at 1 K with different pump frequencies. The bandwidth of the “signal” band can be adjusted significantly by varying the pump frequency. Measurements shown in this sub-figure are from another device on the same wafer with an identical design.

III. RESULTS AND DISCUSSION

A. Behavior

The gain is measured by normalizing the pumped transmission by the pump-off transmission. We expect negligible loss

from the KI-TWPA based on results reported in Shu et al.¹² for a similar device geometry in this frequency range. The KI-TWPA tends to produce gain in disjointed frequency ranges that we refer to as the signal and idler bands (see Fig. 1.a). The amplifier also produces some gain in a narrow frequency band around the pump frequency, but the gain there is less because, in that frequency range, the nonlinear dispersive effect is not compensated by the engineered dispersion. The gap in the gain curve around 12.5 GHz is simply the result of the transmission gap due to the modulation of the stub lengths. The additional gap around 8.7 GHz occurs because with the signal tone near that frequency, the idler tone would fall within the bandgap, and therefore, the gain process is inoperative. The gaps in the gain curve serve a useful function in that it is easier to use a diplexer to separate out the pump and the signal and idler bands. Typically, diplexers have poor input matching at their crossover frequencies, so by placing those frequencies in the zero gain regions, potential problems with reflections can be avoided.

The expected gain of the device was calculated using the low power dispersion extracted from the measured unpumped transmission. The measurement was compared to a network model of the KI-TWPA to determine the film surface inductance. In our method, described in ref.¹², the modulated transmission line is considered to be a uniform medium with an effective dielectric constant, which we derive from the adjusted network model. That effective dielectric constant is used in the coupled-mode equations to predict the gain. For the simulated gain curve shown in Fig. 2.a, the higher-frequency products at $2\omega_p + \omega_s$, $3\omega_p$, and $4\omega_p - \omega_s$ were included in the calculation in addition to the signal, pump and idler frequencies¹². To achieve a similar gain level to the measured value, we adjusted the value of the pump current used in the calculation. Comparing the simulation plot shown in Fig. 2.a indicates a good agreement with measurement results.

The frequency band over which the device produces gain can be tuned significantly by adjusting the frequency of the pump tone, as shown in Fig. 2.b. As the dispersion introduced by the periodic modulation changes rapidly below the bandgap (Fig. 1.b), small pump frequency changes result in somewhat larger changes in the signal and idler frequencies that satisfy the phase matching condition, eqn. 2.

To measure gain compression, a test tone in the middle of the device’s signal band was injected into the KI-TWPA, and the system’s output power was measured using a spectrum analyzer. With the pump frequency set to 10.6 GHz and pump tone power of -23 dBm, resulting in 15 dB of gain, the output power of the amplified test tone at the spectrum analyzer was measured as a function of the test tone’s power at the device. As shown in Fig. 3.a, the gain compresses by 1 dB when the input signal is \simeq -58 dBm, which corresponds to an output power of -43 dBm. As the power of the output signal and idler tones is provided by the pump, compression occurs when the pump is level significantly depleted. For our device, that occurs with an output signal power of about -20 dB below the pump power.

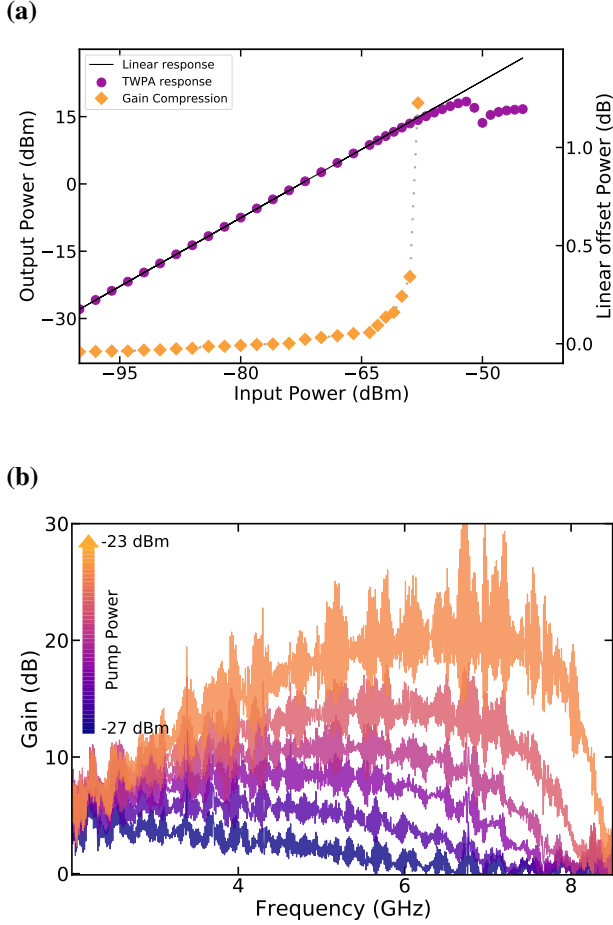


FIG. 3: a) Plot of the measured output power at the spectrum analyzer of a test tone as a function of the test tone's input power at 20 mK with a signal gain of 15 dB. The gain compresses by 1 dB from the linear response when the input signal power reaches -58 dBm. b) Plot of the measured gain for a fixed pump tone frequency as a function of pump tone power at 20 mK. Both of these measurements were taken using the setup shown in Fig. 5. The higher ripple level in this plot compared to Fig. 2.a is due to the addition of more components in the measurement setup, such as the diplexers and more cabling, which can cause impedance mismatch.

B. Noise

The amplifier chain noise was measured using a Y-factor method with two 50Ω cryogenic loads as noise sources, one at 3.18 K and the other at the Mixing Chamber (MXC) stage (~ 20 mK) of the dilution refrigerator. Using a cryogenic relay switch, we alternate between the noise sources as shown in Fig. 4.a. Due to a lack of output-to-input isolation, reflections must be avoided at either side of the TWPA at frequencies where the amplifier has gain. If the sum of the dB return losses on the input and output sides does not exceed the gain, an oscillation will develop. The circuit shown in Fig. 4 pro-

vides an impedance match at both the input and output of the KI-TWPA over the signal and idler frequency ranges using a combination of diplexer (DPX) circuits. The input side diplexers allow for the injection of the pump tone through a band-pass filter (not shown) that removes synthesizer phase noise. The input side DPX I provides a cold termination to the input of the KI-TWPA over the idler band (>13 GHz). The noise from that termination determines the added noise of the KI-TWPA, so it is kept at a temperature $T \sim 20$ mK $\ll \hbar\omega_i/k_B$ for the system to be quantum limited. In this configuration, the KI-TWPA only receives the thermal noise emitted from the calibration sources in the signal band.

On the output side of the KI-TWPA, the diplexer removes the pump and idler tones and terminates them. To minimize heating, the pump is terminated at a higher temperature stage (~ 50 mK). The idler is also terminated at 50 mK to keep the KI-TWPA quantum limited. Finally, an isolator is used to avoid noise from the HEMT, which may otherwise contaminate the KI-TWPA via the same mechanism. The signal is then further amplified using a room temperature amplifier and measured using a spectrum analyzer.

The total noise of the amplifier chain, which includes the KI-TWPA, a Low Noise Factory cryogenic HEMT amplifier (Model: LNF-LNC0.3_14B), and a room temperature low noise amplifier, was determined using the Y-factor method,

$$N_{\text{sys}}(\omega) = \frac{N_H(\omega) - Y N_C(\omega)}{Y - 1}, \quad (3)$$

where ω is the signal angular frequency, k_B is the Boltzmann constant, and \hbar is the reduced Planck's constant. The $N_C(\omega)$ and $N_H(\omega)$ are the noise temperatures of the hot and cold terminations in units of quanta given by²¹

$$N_{H,C} = \frac{1}{2} \coth\left(\frac{\hbar\omega}{2k_B T'_{H,C}}\right) \quad (4)$$

where $T'_{H,C}$ is the physical temperature of the noise sources.

The noise added by the KI-TWPA itself was determined using the measured gain of the device and the total system noise from the Y-factor measurement. Microwave losses in the measurement setup, especially between the KI-TWPA and the noise sources, can cause an overestimation of the measured noise. We estimated the loss from the diplexers by comparing the measured transmission through the KI-TWPA and diplexers to that of a bypass cable as shown in Fig. 5.a. After considering the loss, the added noise, N_A , in units of quanta, of the KI-TWPA can be calculated as

$$N_A = L_1 N_{\text{sys}} - N_{qm} \left(\frac{L_2 G_{PA}(1-L_1) + (1-L_2)}{L_2 G_{PA}} \right) - \frac{N_{HEMT}}{L_2 G_{PA}} \quad (5)$$

where L_1 and L_2 are the losses in the components before and after the KI-TWPA, respectively. $N_{qm} = 0.5$ is the quantum noise, N_{HEMT} is the added noise of the HEMT amplifier and

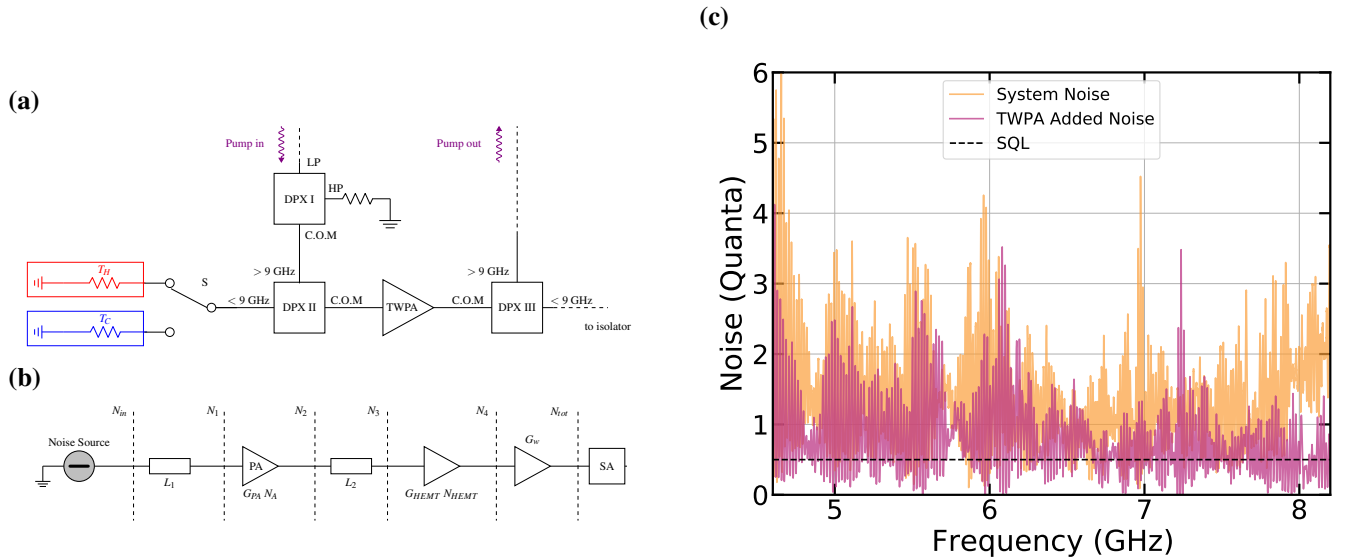


FIG. 4: a) Schematic of the noise measurement setup with hot and cold broadband noise sources. Two 50Ω cryogenic loads were used as noise sources. The hot source was heat sunk to the 3 K stage of the dilution fridge with a base temperature of 3.18 K, and the cold noise source was placed on the fridge’s mixing chamber (MXC) with a base temperature of $\simeq 20$ mK. All other components in this figure were placed in the MXC. Using a relay switch S, the input of the KI-TWPA was switched between the hot and cold sources. The two types of diplexers have crossovers in the lower and upper gaps in the gain curve shown in Fig. 2.a and are used to inject and separate out the pump and idler tones. c) circuit diagram of the cascaded noise model for the KI-TWPA measurement setup.

G_{PA} is the measured gain of the KI-TWPA. The noise model used to arrive at equation (6) is explained in Appendix B. We measure a total system noise of $1 \leq N_{sys} \leq 2$ in the 4.6 - 8.1 GHz range as shown in Fig. 4.c. Using equation (6), we estimate the added noise of the KI-TWPA to be $0.5 \leq N_{sys} \leq 1.5$ as shown in Fig. 4. The cryogenic HEMT amplifier’s noise was measured using the Y-factor with the pump off. We measured an average noise temperature of 5 K or ~ 13 quanta in the 4 - 8 GHz band consistent with data provided in the amplifier’s datasheet. It was observed that the measured added noise in the KI-TWPA deviates from half a quanta in some places (Fig. 4.c). These discrepancies could be attributed to some nonidealities in the test setup. For instance, both noise sources are connected to the input of the KI-TWPA through three cables and two switches. Estimating the insertion loss in all these components is quite challenging, and any unaccounted losses can lead to uncertainty in the measurement and overestimation of the measured noise. Impedance mismatch between the noise terminations and the KI-TWPA is also another source of uncertainty in our noise measurements. The ripples in the measured system noise and the TWPA-added noise are indications of these imperfections.

IV. CONCLUSION

In conclusion, we have designed, fabricated, and measured a wide-bandwidth Four-Wave Mixing KI-TWPA that pro-

duces gain between 3 - 9 GHz with a 1 dB compression of -58 dBm suitable for the readout of large detector arrays and superconducting qubits. Using a Y-factor method, we have demonstrated a near quantum-limited noise performance of KI-TWPA in the 4.6 to 8.1 GHz frequency range. The amplifier produces gain in disjointed frequency ranges that we call the signal band and a higher-frequency idler (or image) band. This makes it straightforward to separate the idler using ancillary circuitry and use the full signal band without contamination from the image (or idler) frequencies for the readout of cryogenic detectors. The signal band peak gain of this device is shown to be tunable with the frequency of the pump tone. This tunability makes the KI-TWPA suitable for applications where the signal frequency range needs to be adjusted, such as in dark matter experiments. In addition, The higher frequency idler band of the KI-TWPA can be used to look for dark matter candidates with a higher mass range, which makes it possible to cover a wide range of masses with a single KI-TWPA.

ACKNOWLEDGMENTS

This research was carried out at the Jet Propulsion Laboratory under a contract with the National Aeronautics and Space Administration (80NM0018D0004). F.F’s research was supported by appointment to the NASA Postdoctoral Program at the Jet Propulsion Laboratory, administered by Oak Ridge Associated Universities under contract with NASA.

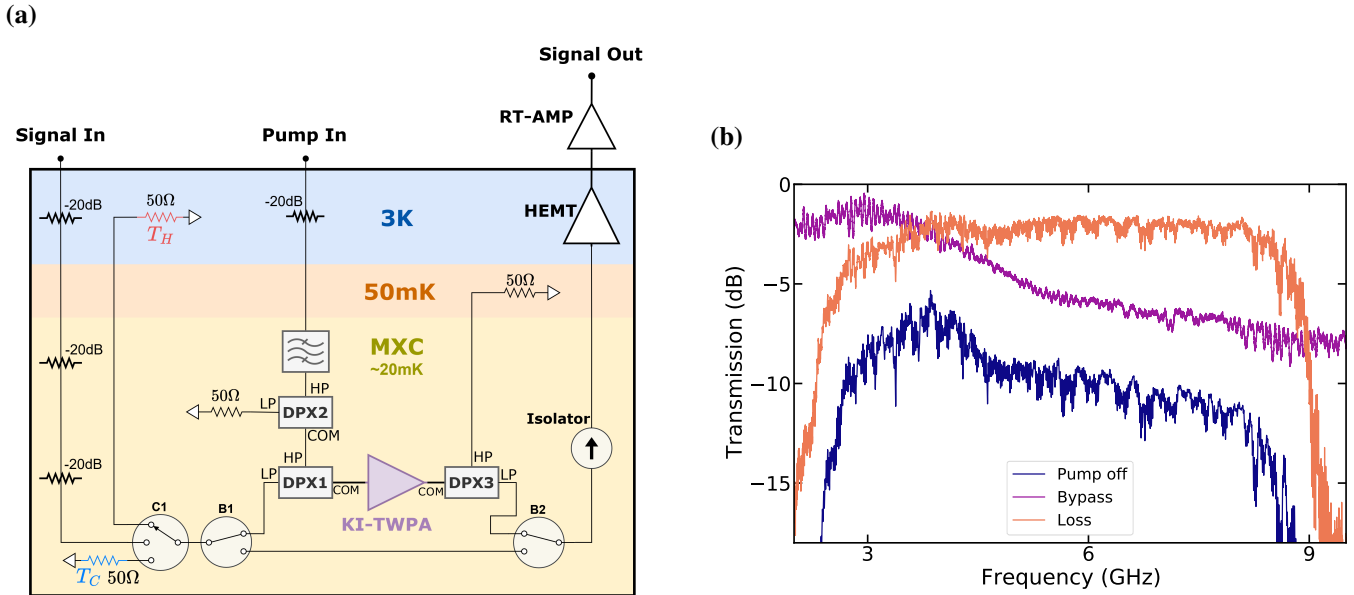


FIG. 5: a) Circuit diagram of the noise measurement setup. The input line is attenuated using three cryogenic attenuators and then connected to switch C1. Two cryogenic 50 Ω loads were used as noise sources. The ‘Hot’ noise source was placed at the 3 K stage of the Dilution fridge, and the ‘Cold’ noise source was placed at the MXC. In this configuration, we can switch between the 50 Ω for Y-factor measurements and the signal line for gain measurements. The Pump tone was injected in the KI-TWPA through a bandpass filter and DPX 1 and 2 with cross-over frequencies of 14 and 9 GHz, respectively. The pump tone is then routed out using DPX 3 (cross-over frequency of 9 GHz) and terminated on the 50 mK stage of the cryostat to prevent the HEMT from saturating. The cables used in the measurement setup connecting switch C1 to the ‘hot’ and ‘cold’ terminations on the 3 K and the MXC stages were NbTi superconducting cables. To calibrate the loss in the components, we used a cryogenic cable between switches B1 and B2 to bypass the TWPA and the diplexers. The output is then read out through an isolator, a cryogenic HEMT amplifier, and a room-temperature amplifier using a spectrum analyzer. b) The plot of measured transmission through the entire noise setup with the KI-TWPA unpumped is denoted as ‘Pump off,’ and through the cryogenic cable bypassing the components is denoted as ‘Bypass.’ The transmission plot labeled ‘Loss’ is the difference between the two measurements divided by two to account for the loss between switch B1 and the KI-TWPA.

Appendix A: Noise Measurement Setup

The input line is sufficiently attenuated from room temperature to the MXC stage using a combination of attenuators placed on the 3 K stage and MXC of the dilution refrigerator. For calibration and y-factor measurements, we utilized three relay switches at the MXC. Switch C_1 (Fig. 5) is used to switch between the input of the cryostat and the hot and cold terminations. Switches B_1 and B_2 are synced up and operated to switch between the KI-TWPA and a cryogenic cable for calibration. The amplified signal then passes through an isolator (on MXC) and a cryogenic HEMT amplifier at the 3 K stage, further amplified by a room temperature low noise amplifier, and finally read out using a spectrum analyzer.

The pump input was filtered using a bandpass filter at the MXC stage and directed to the KI-TWPA using DPX 2 and 1 as illustrated in Fig 5a. Using the highpass port of DPX 3, the pump tone is terminated at the 50 mK stage of the dilution fridge. The total transmission of the system through the device was measured using a VNA with the pump tone off and the transmission of the cable bypassing the KI-TWPA and

the diplexers as shown in Fig. 5.a. The plots comparing the transmission between the cryogenic cable and the unpumped KI-TWPA are shown in Fig. 5.b and labeled as ‘Bypass’ and ‘Pump off,’ respectively. The net loss from DPX 1 placed between the KI-TWPA and switch C1 in the circuit is also plotted in Fig. 5.b as ‘Loss.’

Appendix B: Noise Theory

To model the noise in the setup, we used the circuit diagram shown in Fig. 4.b. If we assume the mK losses in the components between the noise sources (hot & cold in this case) and the KI-TWPA are L_1 and L_2 , the cascaded noise equations can be written as follows:

$$N_1 = L_1 N_{in}(T) + N_{qm}(1 - L_1), \quad (\text{B1})$$

$$N_2 = G_{PA} (N_1 + N_A), \quad (\text{B2})$$

$$N_3 = L_2 N_2 + N_{qm}(1 - L_2), \quad (\text{B3})$$

$$N_4 = G_{HEMT} (N_3 + N_{HEMT}), \quad (\text{B4})$$

$$N_{tot} = G_w N_4. \quad (\text{B5})$$

Where $N_{in}(T) = (1/2) \coth(\hbar\omega/2k_B T)$ is the input noise from the 50Ω terminations. N_{qm} is the quantum noise and for $k_B T \ll \hbar\omega$ is equal to one half. G_{PA}, N_A and G_{HEMT}, N_{HEMT} are the gain and added noise of the KI-TWPA and the HEMT amplifier, respectively. G_w is the additional effective warm amplification, and N_{tot} is the total noise measured on the spectrum analyzer (SA).

When the KI-TWPA is pumped, the total noise measured by the SA can be calculated using equations (B1-B5).

$$N_{tot}^{on} = G_{eff} [N_{in}(T) + N_{PA}^{eff} + N_{HEMT}^{eff}] \quad (\text{B6})$$

where G_{eff}, N_{PA}^{eff} and N_{HEMT}^{eff} are defined as follows.

$$G_{eff} = G_w G_{HEMT} L_2 G_{PA} L_1 \quad (\text{B7})$$

$$N_{PA}^{eff} = \frac{N_{qm}(1 - L_1)}{L_1} + \frac{N_A}{L_1} \quad (\text{B8})$$

$$N_{HEMT}^{eff} = \frac{N_{qm}(1 - L_2)}{L_2 G_{PA} L_1} + \frac{N_{HEMT}}{L_2 G_{PA} L_1} \quad (\text{B9})$$

By switching to a hot and a cold load, therefore varying the input noise, we can extract the system noise

$$N_{sys} = N_{PA}^{eff} + N_{HEMT}^{eff} \quad (\text{B10})$$

When the KI-TWPA is unpumped, we can treat it as a lossless transmission line. Using the cascaded noise equations, we arrive at the following equation for the total noise measured at the SA with the pump off.

$$N_{tot}^{off} = \frac{G_{eff}}{G_{PA}} \left[N_{in}(T) + \frac{N_{qm}(1 - L_1 L_2) + N_{HEMT}}{L_1 L_2} \right] \quad (\text{B11})$$

If we bypass the KI-TWPA and all the components between the noise source and the HEMT amplifier, the total noise measured at SA is

$$N_{tot}^{BP} = G_w G_{HEMT} [N_{in}(T) + N_{HEMT}]. \quad (\text{B12})$$

Then the added noise of the KI-TWPA is

$$N_A = L_1 N_{sys} - N_{qm} \left(\frac{L_2 G_{PA} (1 - L_1) + (1 - L_2)}{L_2 G_{PA}} \right) - \frac{N_{HEMT}}{L_2 G_{PA}} \quad (\text{B13})$$

In the above equations, the loss factors L_1 and L_2 can be estimated either by measuring insertion losses of the components separately or using the bypass and pump-off transmission measurements using the relay switches. N_{HEMT} can be estimated using either equation (B 12) or (B 11) with a y-factor measurement. Finally, measuring the gain of the KI-TWPA, we can calculate the added noise of the TWPA from the above equation. Using the unpumped KI-TWPA noise spectra, we measure an average HEMT noise temperature of 5 kelvin, which is in agreement with LNF-LNC0.3_14B datasheet.

In Fig. 5.b, you can see the transmission (S_{21}) measurements of the cable in two scenarios. The first one is the bypassing of KI-TWPA, represented by the orange line, and the second one is the transmission through DPX2, KI-TWPA, and DPX3, represented by the blue line. We have calculated the loss between switch B1 and the KI-TWPA by subtracting the unpumped measurement from the bypass measurement and dividing it by two since we used identical duplexers with similar insertion loss. This calculated loss is plotted as a green line in Fig. 5.b as a function of frequency, and we have used it as L_1 and L_2 loss factors in the main text.

- ¹N. Zobrist *et al.*, "Wide-band parametric amplifier readout and resolution of optical microwave kinetic inductance detectors," *Applied Physics Letters* **115**, 042601 (2019), https://pubs.aip.org/aip/apl/article-pdf/doi/10.1063/1.5098469/14525680/042601_1_online.pdf.
- ²S. Kempf *et al.*, "Demonstration of a scalable frequency-domain readout of metallic magnetic calorimeters by means of a microwave SQUID multiplexer," *AIP Advances* **7**, 015007 (2017), https://pubs.aip.org/aip/adv/article-pdf/doi/10.1063/1.4973872/12927237/015007_1_online.pdf.
- ³M. Malnou *et al.*, "Improved microwave SQUID multiplexer readout using a kinetic-inductance traveling-wave parametric amplifier," *Applied Physics Letters* **122**, 214001 (2023), https://pubs.aip.org/aip/apl/article-pdf/doi/10.1063/5.0149646/17832018/214001_1_5.0149646.pdf.
- ⁴K. Peng *et al.*, "Floquet-mode traveling-wave parametric amplifiers," *PRX Quantum* **3** (2022), 10.1103/prxquantum.3.020306.
- ⁵S. Barzanjeh, D. P. DiVincenzo, and B. M. Terhal, "Dispersive qubit measurement by interferometry with parametric amplifiers," *Physical Review B* **90** (2014), 10.1103/physrevb.90.134515.
- ⁶N. Didier, A. Kamal, W. D. Oliver, A. Blais, and A. A. Clerk, "Heisenberg-limited qubit read-out with two-mode squeezed light," *Physical Review Letters* **115** (2015), 10.1103/physrevlett.115.093604.
- ⁷K. Ramanathan *et al.*, "Wideband direct detection constraints on hidden photon dark matter with the qualiphid experiment," *Phys. Rev. Lett.* **130**, 231001 (2023).
- ⁸J. Aumentado, "Superconducting parametric amplifiers: The state of the art in josephson parametric amplifiers," *IEEE Microwave Magazine* **21**, 45–59 (2020).
- ⁹M. Esposito *et al.*, "Perspective on traveling wave microwave parametric amplifiers," *Applied Physics Letters* **119** (2021), 10.1063/5.0064892.
- ¹⁰J. Mutus *et al.*, "Design and characterization of a lumped element single-ended superconducting microwave parametric amplifier with on-chip flux bias line," *Applied Physics Letters* **103** (2013).
- ¹¹C. Macklin *et al.*, "A near-quantum-limited josephson traveling-wave parametric amplifier," *Science* **350**, 307–310 (2015), <https://www.science.org/doi/pdf/10.1126/science.aaa8525>.
- ¹²S. Shu, N. Klimovich, B. H. Eom, A. D. Beyer, R. B. Thakur, H. G. Leduc, and P. K. Day, "Nonlinearity and wide-band parametric amplification in a

- (nb,ti)n microstrip transmission line,” *Physical Review Research* **3** (2021), 10.1103/physrevresearch.3.023184.
- ¹³M. Malnou *et al.*, “Three-wave mixing kinetic inductance traveling-wave amplifier with near-quantum-limited noise performance,” *PRX Quantum* **2**, 010302 (2021).
- ¹⁴B. Eom, P. K. Day, H. G. LeDuc, and J. Zmuidzinas, “A wideband, low-noise superconducting amplifier with high dynamic range,” *Nature Physics* **8**, 623–627 (2012).
- ¹⁵L. Ranzani *et al.*, “Kinetic inductance traveling-wave amplifiers for multiplexed qubit readout,” *Applied Physics Letters* **113**, 242602 (2018), https://pubs.aip.org/aip/apl/article-pdf/doi/10.1063/1.5063252/14520906/242602_1_online.pdf.
- ¹⁶M. R. Vissers *et al.*, “Low-noise kinetic inductance traveling-wave amplifier using three-wave mixing,” *Applied Physics Letters* **108**, 012601 (2016), https://pubs.aip.org/aip/apl/article-pdf/doi/10.1063/1.4937922/12854602/012601_1_online.pdf.
- ¹⁷S. Chaudhuri *et al.*, “Broadband parametric amplifiers based on nonlinear kinetic inductance artificial transmission lines,” *Applied Physics Letters* **110**, 152601 (2017), https://pubs.aip.org/aip/apl/article-pdf/doi/10.1063/1.4980102/14495669/152601_1_online.pdf.
- ¹⁸W. Shan, Y. Sekimoto, and T. Noguchi, “Parametric amplification in a superconducting microstrip transmission line,” *IEEE Transactions on Applied Superconductivity* **26**, 1–9 (2016).
- ¹⁹“Development of a broadband nb/tn traveling wave parametric amplifier for mkid readout,” (2014).
- ²⁰N. S. Klimovich, *Traveling wave parametric amplifiers and other nonlinear kinetic inductance devices*, Ph.D. thesis (2022).
- ²¹A. Kerr and M. J. Feldman, “Mma memo 161 receiver noise temperature, the quantum noise limit, and the role of the zero-point fluctuations *,” (1996).